European Journal of Remote Sensing

ISSN: (Print) (Online) Journal homepage: www.tandfonline.com/journals/tejr20

Preliminary analysis of wind and wave retrieval from Chinese 1mC-SAR image

Yu-Hang Zhou, Meng-Yu Hao, Wei-Zeng Shao, Armando Marino, Xin-Gai Song & Xing-Wei Jiang

To cite this article: Yu-Hang Zhou, Meng-Yu Hao, Wei-Zeng Shao, Armando Marino, Xin-Gai Song & Xing-Wei Jiang (2024) Preliminary analysis of wind and wave retrieval from Chinese 1mC-SAR image, European Journal of Remote Sensing, 57:1, 2364706, DOI: 10.1080/22797254.2024.2364706

To link to this article: https://doi.org/10.1080/22797254.2024.2364706

Published online: 13 Jun 2024.

EUROPEAN JOURNAL OF REMOTE SENSING
2024, VOL. 57, NO. 1, 2364706
https://doi.org/10.1080/22797254.2024.2364706

Preliminary analysis of wind and wave retrieval from Chinese 1mC-SAR image

Yu-Hang Zhou[a], Meng-Yu Hao[a], Wei-Zeng Shao[a], Armando Marino[b], Xin-Gai Song[c] and Xing-Wei Jiang[c]

[a]College of Oceanography and Ecological Science, Shanghai Ocean University, Shanghai, China; [b]Natural Sciences, University of Stirling, Stirling, UK; [c]National Satellite Ocean Application Service, Ministry of Natural Resources of the People's Republic of China, Beijing, China

ABSTRACT

Chinese satellite carrying synthetic aperture radar (SAR) with spatial resolution up to 1 m, denoted as 1mC-SAR, is the successor of Gaofen-3 (GF-3). The main purpose of this study is to conduct the preliminary analysis of wind and wave retrieval from more than 400 1mC-SAR images acquired in quad-polarization stripmap (QPS), which are located at China coastal waters on April 2023. The co-polarized (vertical–vertical [VV] and horizontal–horizontal [HH]) geophysical model function (GMF), denoted as CSARMOD-GF, is employed for wind speed retrieval from those images taking prior information on wind directions from European Centre for Medium-Range Weather Forecasts (ECMWF). Validation against the wind products from Haiyang-2 (HY-2) (2B/2C/2D) scatterometers yields a 1.78/1.91 m/s root mean squared error (RMSE) with a 0.22/0.23 scatter index (SI) for SAR retrievals at VV/HH polarization channels. Moreover, the accuracy of SAR-derived winds at spatial resolution of 2 km for QPS-I and 6 km for QPS-II is relatively higher than that achieved from the retrievals at spatial resolution of 4 km for QPS-I and 12 km. The wave slop spectrum is inverted from co-polarized image by polarimetric technique, in which the term of wind speed is included in the model transfer function (MTF) of tilt modulation. Significant wave height (SWH) retrievals are compared with the simulations by the third-generation numeric wave model, denoted as WAVEWATCH-III (WW3), showing a 0.53 m RMSE with a 0.36 SI. This behavior is also confirmed as comparing with SAR-derived wave spectra and WW3-simulated wave spectra, i.e. a 0.79 correlation coefficient (Cor) and a 0.92 squared error (Err). The variation of bias in wind speed and SWH indicates an increasing tendency with the growth of sea state, meaning that calibration is a heedful issue for 1mC-SAR.

ARTICLE HISTORY
Received 15 January 2024
Revised 1 April 2024
Accepted 3 June 2024

KEYWORDS
Wind; wave; 1mC-SAR

Introduction

At present, remote sensing is an advanced technique for upper oceanic dynamics monitoring over global seas. For instance, significant wave height (SWH) is measured by altimeter (Shao, Jiang, et al., 2021a). The wave spectrum can be retrieved from synthetic aperture radar (SAR) (Shao, Jiang, et al., 2022a) and wave spectrometer (Surface Wave Investigation and Monitoring, SWIM) (Hao, Shao, Shi, et al., 2023a), especially at extreme sea state (Shao et al., 2020). The spatial resolution of SAR-derived wave spectrum is 1–3 km (Zhong et al., 2023), which is better than an 18 km spatial resolution of wave spectrum measured by SWIM. In this sense, SWIM data is popularly used for analyzing wave characteristic in large scale (Yao et al., 2023), while SAR wave retrievals are beneficial to oceanography at coastal waters (Shao et al., 2023) and polar region (Shao, Zhao, et al., 2022b).

During the Seasat mission in 1978, it has been revealed that sea surface dynamics and target are detectable by SAR via Bragg backscattering mechanism (Alpers & Bruning, 1986), that is, the electromagnetic wave resonant with gravity waves generated by sea surface wind. A strong dependence between sea state and azimuth scattering effects has been demonstrated using ERS-1/2 wave model data (Kerbaol et al., 1998). At moderate radar incidence angle (i.e. 20°–60°), the sea surface backscattering signal represented by normalized radar cross section (NRCS) in co-polarization (vertical-vertical [VV] and horizontal-horizontal [HH]) has linear relation with wind speed up to 25 m s^{-1}, and this is also applicable for scatterometer (Long & Mendel, 1991) and SAR (Grieco et al., 2015; Migliaccio & Reppucci, 2006; Portabella et al., 2002). A geophysical model function (GMF) at C-band (~5.3 GHz) relating with NRCS and a wind vector was originally designed for wind retrieval from scatterometer, i.e. CMOD4 (Stoffelen & Anderson, 1997), CMOD-IFR developed at French Research Institute for Exploitation of the Oceans (IFREMER) (Quilfen et al., 1998) and CMOD5 (Hersbach et al., 2007). The latest version of CMOD family is CMOD7 (Stoffelen et al., 2017) that is a look-table avoiding errors during model fitting process. With the accumulation of SAR data, the GMFs at C-band is directly developed through collocated dataset consisting of

CONTACT Wei-Zeng Shao wzshao@shou.edu.cn College of Oceanography and Ecological Science, Shanghai Ocean University, No.999, Huchenghuan Rd, Nanhui New City, Shanghai, China

SAR image and winds from moored buoys or European Center for Medium Weather Forecasting (ECMWF), i.e. C-SARMOD2 for Sentinel-1 (S-1) (Lu et al., 2018) and CSARMOD-GF for Chinese Gaofen-3 (GF-3) (Shao, Nunziata, et al., 2021b). Recently, a few studies have been conducted for wind speed retrieval through the Doppler shift of C-band radar return signals from the ocean (Mouche, Collard, et al., 2017) and the azimuth cutoff wavelength (Corcione et al., 2018; Grieco et al., 2016). In addition, an empirical algorithm was proposed to retrieve the wind speed based on the co- and cross-polarized SAR measurements (Mouche, Chapron, et al., 2017). In previous studies, it is found that error of SAR-derived wind speed by co-polarized GMFs is within 2 m s^{-1} as validated against the wind product of scatterometer (Shao et al., 2019) or the measurements from National Data Buoy Center (NDBC) buoys (Yang et al., 2011). At wind speed >25 m s^{-1}, the SAR-measured NRCS suffers saturation problem in tropical cyclone (TC) (Hu et al., 2023). Thus, NRCS in vertical-horizontal (VH) polarization that is independent with wind direction is used for TC wind retrieval (Gao et al., 2021; G. S. Zhang et al., 2017), and the accuracy of wind speed is 3–5 m s^{-1} with maximum wind speed up to 70 m s^{-1} (Lai et al., 2023; Zhao et al., 2023).

SAR wave retrieval algorithms include two approaches: theoretical-based algorithm based on the wave mapping mechanism, i.e. tilt, hydrodynamic modulation (Keller & Wright, 1975), and velocity bunching (Alpers & Bruning, 1986); and empirical and machine learning-based models relating SAR-measured variables with wave parameters (Li et al., 2010; Wang et al., 2022). Based on a quasi-linear approximation, the model transfer functions (MTFs) of the above modulations are derived, which are the function of radar incidence angle. Recently, the MTFs of tilt (Y. Zhang et al., 2020) and velocity bunching (Hao, Shao, Yao, et al., 2023b) are significantly improved, in which the term of wind is included. The first SAR wave retrieval algorithm is called the Max-Planck Institute Algorithm (MPI) (Hasselmann & Hasselmann, 1991), which proposes a method for solving wave spectrum through SAR intensity spectrum as employing the first-guess wave spectrum from a numeric model. In the scheme of a semi-parametric retrieval algorithm (SPRA) (Mastenbroek & Valk, 2000) and parameterized first-guess spectrum method (PFSM) (Jiang et al., 2023; J. Sun & Guan, 2006), the first-guess wave spectrum is generated by a parametric wave function (i.e. the Joint North Sea Wave Project model [JONSWAP]) (Shao, Jiang, et al., 2022a), in which the wind retrieved from SAR or scatterometer is used. Additionally, the partition rescaling and shift algorithm (PARSA) (Schulz-Stellenfleth et al., 2005) is specifically designed for wave retrieval utilizing the SAR look-cross spectrum, and the polarimetric technique can be implemented for fully polarimetric SAR data (He et al., 2006). In the literature, the magnitude of capillary wave determines the retune energy backscattered from the sea surface. It has been revealed that SWH has linear relation with NRCS qualitatively associated with tilt and hydrodynamic modulation (Ji et al., 2018) and azimuthal cutoff wavelength representing the velocity bunching (Hao, Shao, Yao, et al., 2023b). Following this rationale, several empirical models have been developed for various C-band SARs, i.e. Envisat-ASAR (Li et al., 2011), S-1 (Stopa & Mouche, 2017) and GF-3 (Zhu et al., 2018). As confirmed in recent studies (Pleskachevsky et al., 2022), the machine learning is also a promising technique for constructing the SAR wave retrieval algorithm.

Since April 2023, Chinese SAR satellite that is the successor of GF-3 (Z. F. Sun et al., 2022), denoted as 1mC-SAR, starts distributing data for domestic investigator. In this study, the main purpose is to confirm the applicability of wind and wave retrieval from 1mC-SAR image. The remainder of this study is organized as follows: Dataset gives the description of the dataset, including the 1mC-SAR images, European Centre for Medium-Range Weather Forecasts (ECMWF), the wind speed from the Haiyang-2 (HY-2) constellation and simulations from the third-generation numeric wave model WAVEWATCH-III (WW3). The methodology of GMF for SAR wind and polarimetric technique for SAR wave retrieval are introduced in Methodology. The validation and error analysis are discussed in Results and discussion. At last, the conclusions are summarized in Conclusions.

Dataset

The description of 1mC-SAR images as well as ECMWF reanalysis (ERA-5) data is first introduced in this section. Then the SWH measurements from HY-2 (2B/2C/2D) and wave simulation by WW3 are briefly described.

1mC-SAR image

The satellite 1mC-SAR was launched on November 2021 and starts distributing data after 1 year of satellite in orbit testing. The technical parameters of 1mC-SAR are listed in Table 1. In this study, the images located at China coastal waters are collected on April 2023. These images are acquired in quad-polarization stripmap (QPS)-I/II mode. The calibration method is as same as that for GF-3 (Zhu et al., 2020):

wherein σ^0 is the NRCS; *DN* is the value of SAR intensity; and *M* and *N* are the constants companied with SAR raw data. As a case show, Figure 1 depicts the calibrated image on 9 April 2023 at 21:57 UTC, i.e.,

Table 1. Technical parameters of 1mC-SAR.

Satellite Altitude			755 km	
Frequency of Electromagnetic Wave			5.3 GHz	
Conventional Incidence Angle			20°–50°	
Extended Incidence Angle			10°–60°	
Imaging Mode		Resolution/m	Swath/m	Polarization
Spotlight Mode		1	10	Single-pol
Stripmap Mode	Ultra Fine Stripmap	3	30	Single-pol
	Fine Stripmap-I	5	50	Dual-pol
	Fine Stripmap-II	10	100	Dual-pol
	Standard Stripmap	25	130	Dual-pol
	Quad-Polarization Stripmap-I	8	30	Full-pol
	Quad-Polarization Stripmap-II	25	40	Full-pol
TOPSAR Mode	Narrow Scan	50	300	Dual-pol
	Wide Scan	100	500	Dual-pol
	Global Observing	500	650	Dual-pol
Wave Mode		8	20	Full-pol
Extended Mode	Low Incidence Angle	25	130	Dual-pol
	High Incidence Angle	25	80	Dual-pol

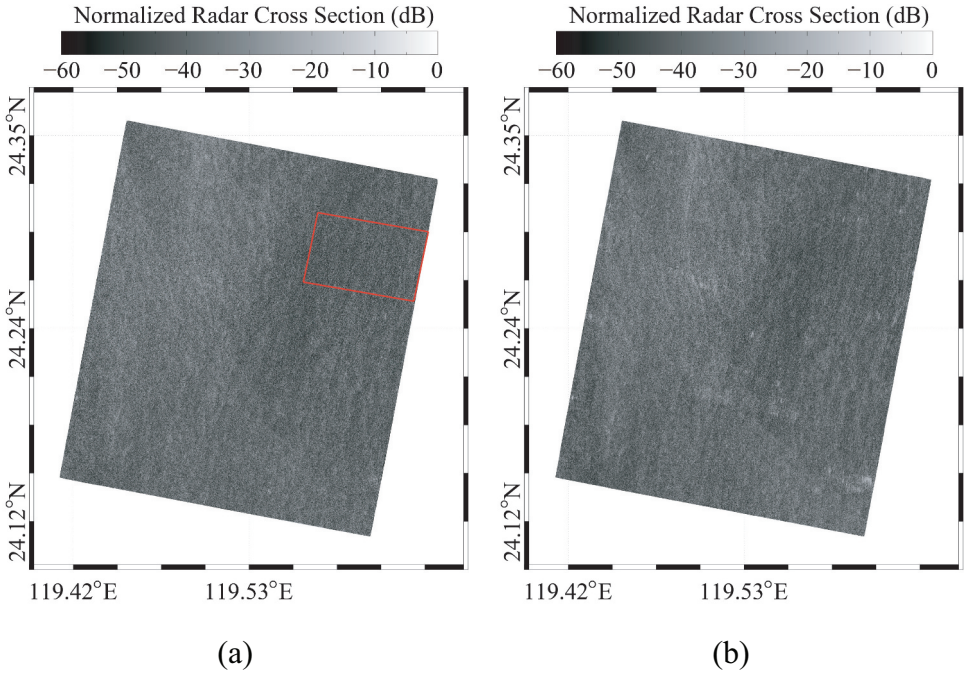

Figure 1. Normalized radar cross-section (NRCS) map of 1mC-SAR synthetic aperture radar (SAR) image on 9 April 2023 at 21:57 UTC: (a) vertical–vertical (VV) and (b) horizontal–horizontal (HH) polarization.

(a) VV-polarization and (b) HH-polarization. The whole image is divided into 256 × 256 pixel sub-scenes with a spatial coverage of 2 km for QPS-I and 6 km for QPS-II and then the sub-scenes are smoothed using a 3 × 3 Gaussian filter.

It is recognized that the pattern on the two-dimensional SAR image spectrum at 800–3000 m length is vertical to the true wind direction (Shao et al., 2023); however, there is 180° ambiguity of SAR-derived wind direction by using the two-dimensional Fast Fourier Transform (FFT-2). In this sense, the prior information on wind direction from ERA-5 at 0.25° grid is employed to remove that ambiguity. Figure 2(a) shows the sub-scene as highlighted by red rectangle in Figure 1(a). The corresponding SAR intensity spectrum at length of 1–3 km is displayed in Figure 2(a), where the red arrow represents the SAR-derived wind direction after taking the ERA-5 wind vector on 9 April 2023 at 22:00 UTC (Figure 3).

HY-2

HY-2B satellite carrying scatterometer and altimeter operates since 2019 and then its sisters HY-2C and HY-2D are continuously launched. In our previous study (Shao, Jiang, et al., 2021a), the statistical analysis shows that the RMSE for wind speed (ASCAT and HY-2B) and for SWH (Jason-3 and HY-2B) is 0.78 m/s and 0.29 m. It is confirmed that wind speed and SWH products from HY-2B that proceeded as geophysical

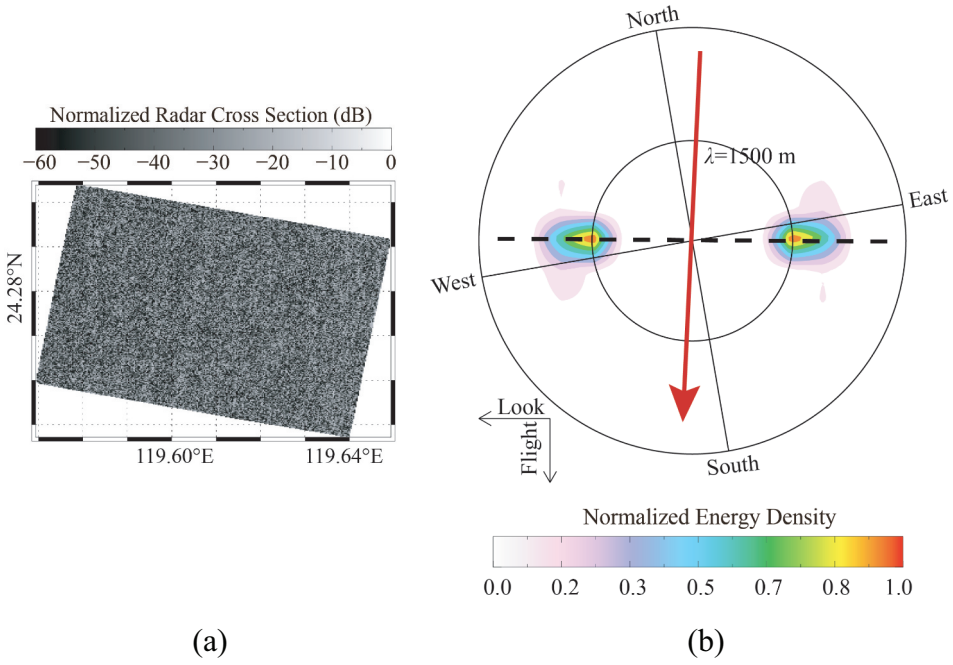

Figure 2. (a) The sub-scene extracted from image at red rectangle in Figure 1a. (b) The corresponding SAR intensity spectrum by using the two-dimensional Fast Fourier Transform (FFT-2) at length of 1–3 km, where the red arrow represents the SAR-derived wind direction.

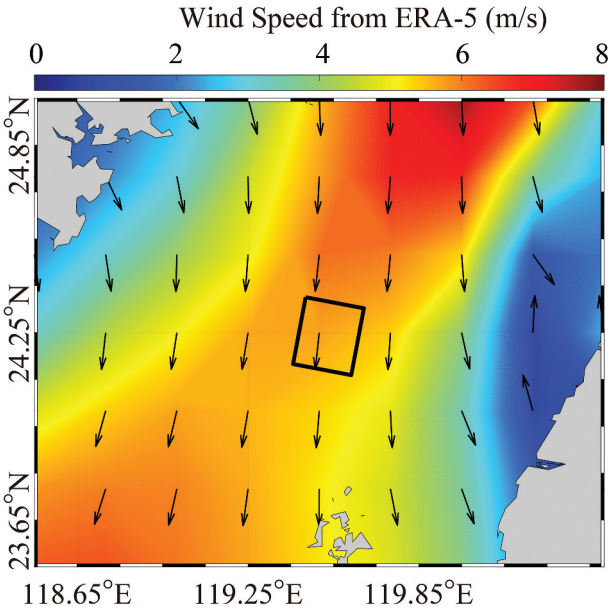

Figure 3. Wind map from European Centre for Medium-Range Weather Forecasts (ECMWF) reanalysis (ERA-5) data on 9 April 2023 at 22:00 UTC.

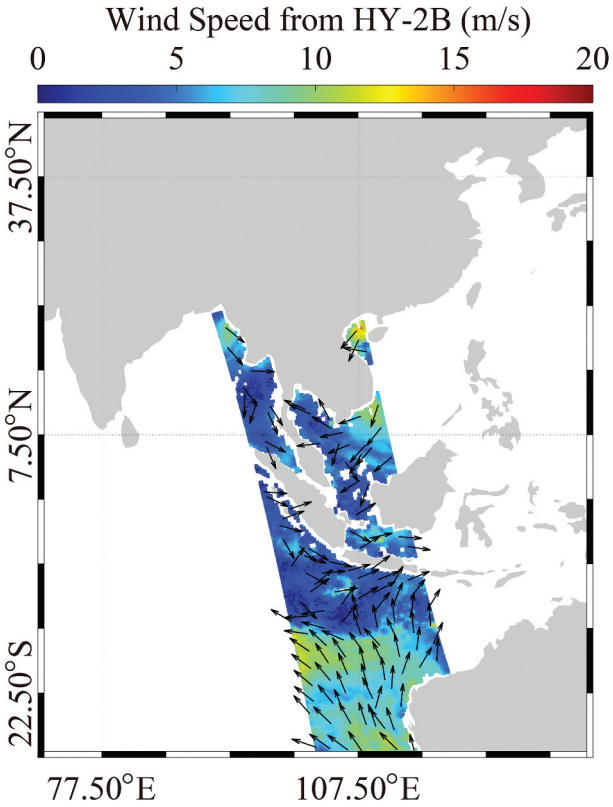

Figure 4. Wind map from Haiyang-2B (HY-2B) scatterometer on 8 April 2023 at 10:41–12:26 UTC.

data records (GDRs) are quite reliable. As well as SAR, the footprint of SWIM onboard CFOSAT has a spatial coverage of 18 × 18 km in a spiral direction of 360°, and SWIM provides the wave product at incidence angles of 6°, 8° and 10° following the footprint. It is concluded in Hao, Shao, Yao, et al. (2023b) that the wave product at incidence angle of 10° has the best performance through the comparison with the simulation by Simulating Waves Nearshore (SWAN). Fortunately, there is no available SWH derived from HY-2 and Jason-2/3 altimeters and wave spectra from SWIM at the SAR acquisition moments. However, the GDRs products of HY-2B/2C/2D scatterometers are used for validation of SAR wind in this study. It should be noted that the time difference between SAR acquisition moments is within 3 h and the distance between them is less than 5 km.

Figure 4 shows the wind map from HY-2B scatterometer on 8 April 2023 at 10:41–12:26 UTC.

Simulations from WW3

Numeric models are popularly applied for predicting and hindcasting sea surface waves, especially at extreme sea state (Shao et al., 2020). As revealed in previous studies (Hao, Shao, Yao, et al., 2023b; Sun et al., 2022), wave simulation from WW3 (WAVEWATCH III Development Group, 2019) has been used as auxiliary data in the SAR oceanography. Here, ERA-5 winds at 0.25° grids and 1-hour intervals are treated as the forcing fields in the WW3 using the default settings. The simulated region is 40°N, 85°N latitude 0°E, 360°E longitude and the time is on April–May 2023. The water depths are derived from the General Bathymetric Chart of the Oceans (GEBCO) bathymetric data, that is smoothed to be ~1-km horizontal resolution. The spatial resolution of outputs from WW3 is 0.05° at intervals of 0.5 h. Although there are no HY-2 footprints passing the spatial coverage of collected 1mC-SAR SAR images, SWHs measured by HY-2 are used to validate the WW3 simulations. Figure 5 presents WW3-simulated SWH map on 10 April 2023 at 21:30 UTC, in which the color spots represent the measurements from HY-2B altimeter. In this case, the pattern of WW3-simulated SWH is consistent with that from HY-2B. Two metric parameters, i.e. a root mean squared error (RMSE) (Equation (1)) and scatter index (SI) (Equation (2)), are used for error analysis between scalars, i.e. wind speed and SWH inverted from SAR image and model simulation.

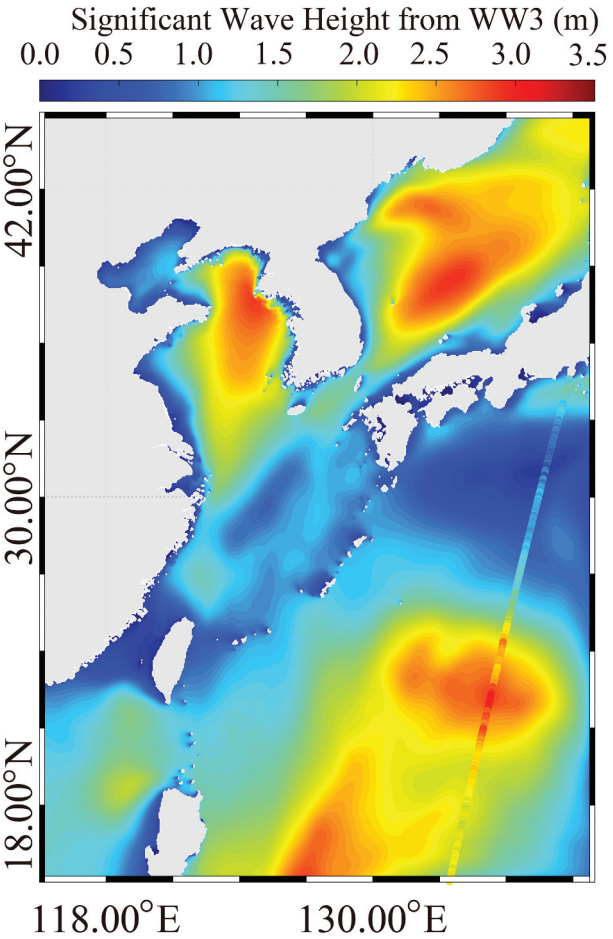

Figure 5. Significant wave height (SWH) map from WAVEWATCH-III (WW3) on 10 April 2023 at 21:30 UTC, in which the color spots represent the measurements from HY-2B altimeter.

$$\mathrm{RMSE} = \sqrt{\frac{1}{n}\sum_{i=1}^{n}(X_i - Y_i)^2} \tag{1}$$

$$SI = \frac{1}{\overline{Y}}\sqrt{\frac{\sum_{i=1}^{n}[(X_i - \overline{X}) - (Y_i - \overline{Y})]^2}{n}} \tag{2}$$

in which, n-elements X_i and $\overline{X}$ represent the SAR retrievals and its average value; and Y_i and $\overline{Y}$ represent the observations and its average value. Figure 6 displays the statistical analysis of WW3-simulated SWH for a 0.1 m bin, indicating a 0.40 m RMSE and a 0.35 SI. Table 2 shows the comprehensive evaluation results of the simulated Significant wave height simulated by WW3 under different sea states. It is worth noting that most of the data sets come from low sea states (0 ~ 1.5 m). Although the RMSE of SWH is higher at high sea states (>3 m), the statistical results of the entire data set are satisfactory under three different sea state conditions. Therefore, we think the simulations from WW3 is reliable.

Methodology

In this section, the methodology for SAR wind and wave retrieval is briefly presented. In particular, the novel tilt MTF used in SAR wave retrieval algorithm is described. Additionally, two metric parameters for error analysis wave spectrum are exhibited.

GMF for SAR wind retrieval

According to Bragg backscattering theory, the SAR roughness is correlated with the magnitude of capillary wave; on the contrary, the distribution of sea surface wave is determined by wind and sea fetch. It is reasonable that backscattering signal linearly relates with wind speed, and this is confirmed through analyzing the scatterometer-measured NRCS with respect to ECMWF wind (Stoffelen & Anderson, 1997). Based on the finding, GMF relating NRCS with a wind vector and incidence angle θ is stated as:

$$\sigma^0 = 1 + B_1(U_{10},\theta)\cos\varphi + B_2(U_{10},\theta)\cos 2\varphi \tag{3}$$

in which σ^0 is the linear NRCS; U_{10} is the sea surface wind speed at 10 m height; θ is radar incidence angle;

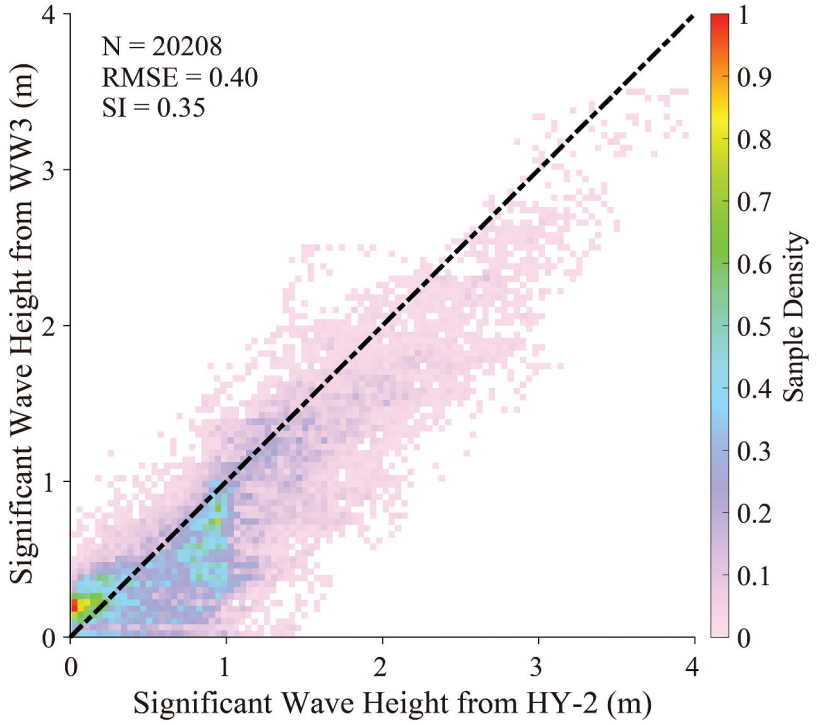

Figure 6. Comparison of SWH between WW3 simulations and HY-2 altimeters for a 0.1 m bin.

Table 2. Statistical analysis of significant wave heights simulated by WW3 versus the measurements from Hiayang-2 (HY-2) altimeters.

			Evaluation Metrics	
Wave Parameters	Sea States	Sample Numbers	SI	RMSE
Significant wave height	0 ~ 1.5 m	16571	0.4315	0.3285
	1.5 ~ 3 m	3468	0.1173	0.4540
	>3 m	169	0.0930	0.4952
	Total	20208	0.3468	0.4008

and φ is wind direction relative to flight orientation. After knowing wind direction, wind speed is conveniently retrieved from SAR image. In previous study (Shao, Nunziata, et al., 2021b), CSARMOD-GF is specifically adopted for co-polarized (VV and HH) GF-3 based on the formulation of C-SARMOD2. Because the calibration method of 1mC-SAR is same to that of GF-3, CSARMOD-GF is directly used here. It is recognized that noise floor is also an essential issue for SAR wind retrieval, especially for cross-polarization. However, there are limited 1mC-SAR images available for this study, which is insufficient for analyzing the noise floor. Therefore, the noise floor is not discussed here.

Polarimetric technique for SAR wave retrieval

In the literature, hydrodynamic modulation and velocity bunching keep unchanged under different polarizations. Therefore, the variation in the difference of backscattering cross section modulation between polarization orientation ϕ and co-polarization is expressed as follows (Zhu et al., 2018):

$$\frac{\Delta\sigma_0^{\phi}}{\bar{\sigma}_0^{\phi}} - \frac{\Delta\sigma_0^{\mathrm{vv}}}{\bar{\sigma}_0^{\mathrm{vv}}} = (T_{\phi}^{tilt} - T_{\mathrm{vv}}^{tilt})\frac{\partial\xi}{\partial\mathbf{r}} \tag{4}$$

$$\frac{\Delta\sigma_0^{\phi}}{\bar{\sigma}_0^{\phi}} - \frac{\Delta\sigma_0^{\mathrm{hh}}}{\bar{\sigma}_0^{\mathrm{hh}}} = (T_{\phi}^{tilt} - T_{\mathrm{hh}}^{tilt})\frac{\partial\xi}{\partial\mathbf{r}} \tag{5}$$

where

$$\sigma_0^{\phi} = \frac{1}{4}(\sigma_0^{\mathrm{hh}} + \sigma_0^{\mathrm{vv}})(1 + \cos^2 2\phi)1mu + 1mu\frac{1}{2}(\sigma_0^{\mathrm{hh}}\sigma_0^{\mathrm{vv}})\cos 2\phi + \sigma_0^{\mathrm{hv}} + \frac{1}{2} \times \Re(\sigma_0^{\mathrm{hhvv}}) \times \sin^2 2\phi \tag{6}$$

in which $\Re(\sigma_0^{\mathrm{hhvv}})$ is the real parts of the correlation between VV-polarized NRCS σ_0^{vv} and HH-polarized NRCS σ_0^{hh}; σ_0^{hv} is the NRCS in horizontal–vertical (HV) polarization; $\partial\xi/\partial\mathbf{r}$ represents the partial derivative of wave slop ξ relative to slant direction $\mathbf{r}$; and T_{ϕ}^{tilt} is the tilt MTF at polarization orientation ϕ, i.e. polarization orientation in VV ($\phi = 90°$) and HH polarization ($\phi = 0°$). The tilt MTF is decomposed into two components perpendicular to (k_x) and parallel to (k_l) the radar look direction, which will be described in later section. Therefore, the expressions can be simplified as follows:

$$\frac{\Delta\sigma_0^{\phi}}{\bar{\sigma}_0^{\phi}}-\frac{\Delta\sigma_0^{\mathrm{vv}}}{\bar{\sigma}_0^{\mathrm{vv}}}=(T_{k_l,\phi}^{tilt}-T_{k_{l,\mathrm{vv}}}^{tilt})\frac{\partial\xi}{\partial l}+(T_{k_x,\phi}^{tilt}-T_{k_{x,\mathrm{vv}}}^{tilt})\frac{\partial\xi}{\partial x} \tag{7}$$

$$\frac{\Delta\sigma_0^{\phi}}{\bar{\sigma}_0^{\phi}}-\frac{\Delta\sigma_0^{\mathrm{hh}}}{\bar{\sigma}_0^{\mathrm{hh}}}=(T_{k_l,\phi}^{tilt}-T_{k_{l,hh}}^{tilt})\frac{\partial\xi}{\partial l}+(T_{k_x,\phi}^{tilt}-T_{k_{x,\mathrm{hh}}}^{tilt})\frac{\partial\xi}{\partial x} \tag{8}$$

in which $\partial\xi/\partial l$ and $\partial\xi/\partial x$ represents the wave slop in the range and azimuth directions, respectively. The SWH H_s is practically calculated by root mean square slop S_{rms} (Equation (10)) and the wave-slop direction ψ.

$$H_s=2\sqrt{2}\times S_{rms} \tag{9}$$

$$S_{rms}=\sqrt{\left(\left\langle\frac{\partial\xi}{\partial l}\times\ \sin\psi\right\rangle\right)^2+\left(\left\langle\frac{\partial\xi}{\partial x}\times\ \cos\psi\right\rangle\right)^2} \tag{10}$$

Collectively, the diagrammatic sketch of this study is illustrated in detail in Figure 7.

MTF of tilt modulation

It is well known that the tilt modulation represents the variation in the NRCS in terms of radar incidence angle. Tilt MTF at polarization orientation ϕ is the sum of two components in k_x and k_l direction:

$$T_{\phi}^{tilt}=ik_lA+ik^xB \tag{11}$$

in which $i=\sqrt{-1}$; and A and B are the complex coefficients. As known in He, the components of the tilt MTF at polarization orientation ϕ in the radar look direction k_l and radar flight direction k_x have the formulations:

$$T_{k_l,\phi}^{tilt}=\frac{ik_l}{M}\left(4\frac{1+\cos^2 2\phi}{\sin 2\theta\cos^2\theta}-8\frac{\tan^2\theta\cos 2\phi}{\sin 2\theta}+2\frac{\sin^2 2\phi}{\cos^3\theta\ \sin\theta}\right) \tag{12}$$

$$T_{k_x,\phi}^{tilt}=-\frac{ik_x}{M}\frac{\sin 2\phi}{\sin\theta}\left\{\left[1+\left(\frac{1+\sin^2\theta}{\cos^2\theta}\right)^2\right]\cos 2\phi+\left[1-\left(\frac{1+\sin^2\theta}{\cos^2\theta}\right)^2\right]-2\left(\frac{1+\sin^2\theta}{\cos^2\theta}\right)\cos 2\phi\right\} \tag{13}$$

where

$$\mathrm{M}=\frac{1}{4}\left[1+\left(\frac{1+\sin^2\theta}{\cos^2\theta}\right)^2\right](1+\cos^2 2\phi)\frac{1}{2}(1+\tan^2\theta)\sin^2 2\phi-2\frac{1+\sin^2\theta}{\cos 4\theta}\cos 2\phi \tag{14}$$

Because the coefficient B is assumed to be zero in VV and HH polarization, the c-polarized MTFs of tilt modulation are reduced to be theoretical expressions of incidence angle (Hasselmann & Hasselmann, 1991). In recent work (Zhang et al., 2021), reanalysis tilt MTF including both radar incidence angle θ and wind speed U_{10} is proposed based on C-band GMF.

$$T_{pp}^{tilt}=ik_l(a_1U_{10}^2+a_2\varphi^2+a_3\theta^2+a_4U_{10}\varphi+a_5U_{10}\theta+a_6\theta\varphi+a_7U_{10}+a_8\varphi+a_9\theta+a_{10}) \tag{15}$$

in which k_l is the wave number in radar look direction; i is an imaginary number; pp denotes the VV or HH polarization; and the values of matrix a are listed in Table 3. The reanalysis tilt MTF has been implemented for wave retrieval from quad-polarized GF-3 image by the polarimetric technique (Shao et al., 2023), in which ϕ is set as 45° in Equations (12)–(14).

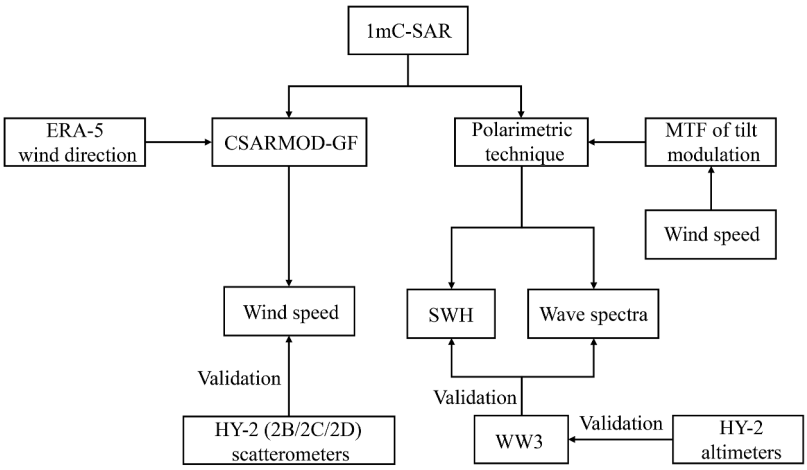

Figure 7. The diagrammatic sketch of this study.

Table 3. Values of coefficients in Equation (5) in vertical–vertical (VV) and horizontal–horizontal (HH) polarization.

Coefficient	VV	HH
a_1	0.007799	0.008398
a_2	1.21723e−15	1.226019e−05
a_3	0.002941	0.005492
a_4	−3.635699e−14	5.00855e−15
a_5	0.008508	0.008506
a_6	−3.365627e−14	8.150555e−15
a_7	−0.685241	−0.714355
a_8	1.303660e−12	−3.285571e−13
a_9	−0.595169	−0.792862
a_{10}	29.084355	30.901273

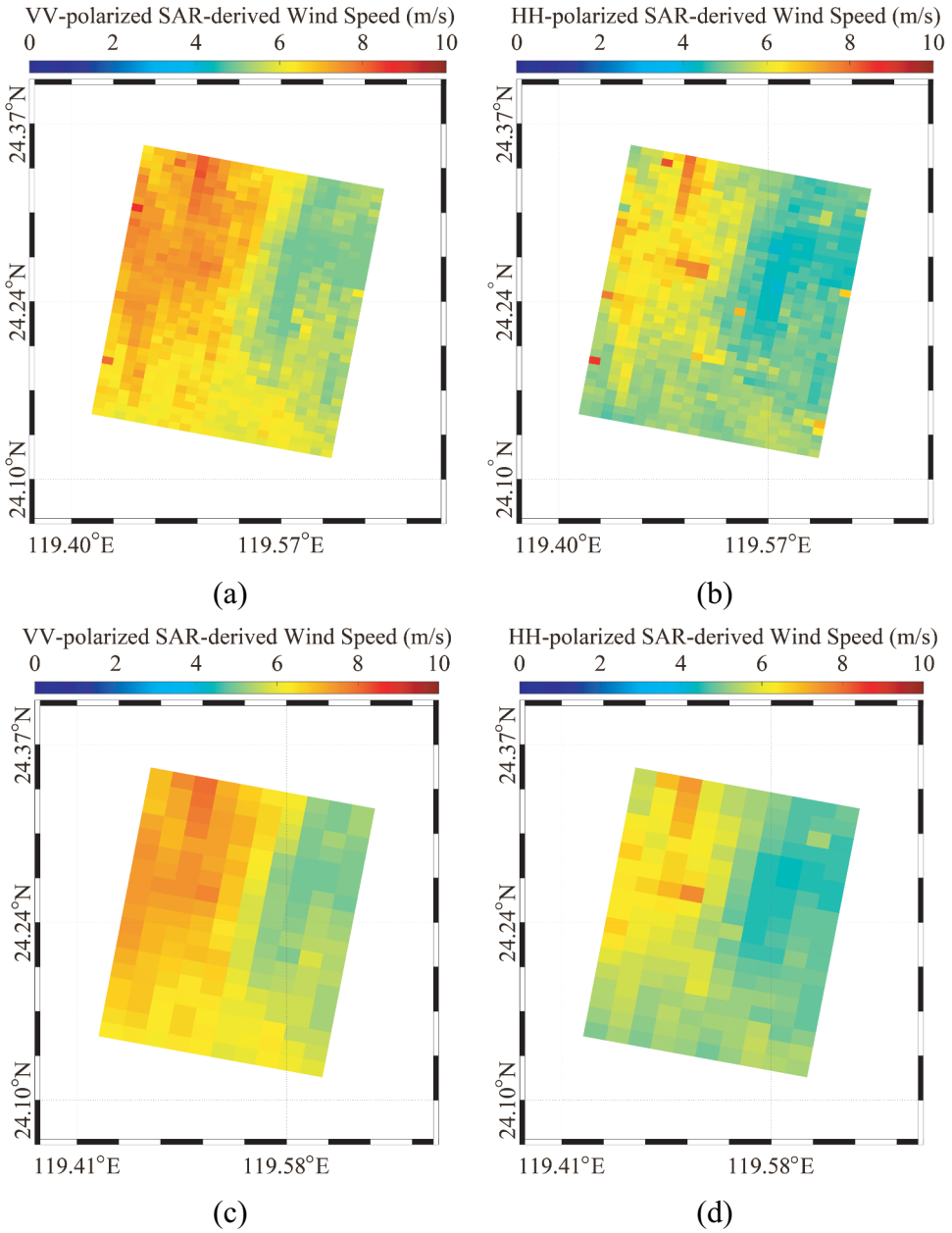

Figure 8. Wind speed retrieval maps corresponding to the (a) VV-polarized image by 256 × 256 sub-scenes and (c) VV-polarized image by 512 × 512 sub-scenes in Figure 1a; (b) HH-polarized image by 256 × 256 sub-scenes and (d) HH-polarized image by 512 × 512 sub-scenes in Figure 1b.

Metric parameters

In order to compare the wave spectrum between SAR retrievals and WW3 simulation, the correlation coefficient (Cor) (Equation (16)) and the squared error (Err) (Equation (17)) are employed, in which k is the wave number. It is necessary to figure out that the wave spectra of two sources are similar with Cor approaching 1 and becomes smaller than that of Err. These two parameters have been taken for analyzing the accuracy of numerical simulation of ocean waves in recent studies (Hao, Shao, Shi, et al., 2023a; Yao et al., 2023).

$$\mathrm{Cor} = \frac{\sum P_k Q_k \Delta k}{\sqrt{\sum P_k^2 Q_k^2 \Delta k}} \tag{16}$$

$$\mathrm{Err} = \frac{\sum (P_k - Q_k)^2 \Delta k}{\sqrt{\sum P_k^2 \Delta k \sum Q_k^2 \Delta k}} \tag{17}$$

It should be noted that the SAR-derived wave slop spectrum $\xi(k)$ has to be converted into wave spectrum $\psi(k)$ that is consistent with simulation from WW3. The method follows the equation below.

$$\xi(k) = k^2 \psi(k) \tag{18}$$

Results and discussion

The accuracy of co-polarized SAR wind retrieval is first presented as validated against wind speeds from HY-2 scatterometers. Then SAR wave retrievals are compared with the SWHs from HY-2 altimeters and wave spectra simulated by WW3. At last, the error analysis is conducted.

Validation of wind retrieval

Co-polarized GMF, namely CSARMOD-GF, is implemented for VV-polarized and HH-polarized image, and the wind retrieval maps with different spatial grid corresponding to the image in Figure 1 (a,b) are shown in Figure 8, i.e. Figures 8(a,b) by 256×256 sub-scenes (i.e. 2 km for QPS-I and 6 km) and Figures 8(c,d) by 512×512 sub-scenes (i.e. 4 km for QPS-I and 12 km) respectively. Although the pattern of VV-polarized wind retrievals is consistent with that of HH-polarized wind retrievals, there is slight difference between them. With the spatial grid increasing, the accuracy of wind speed

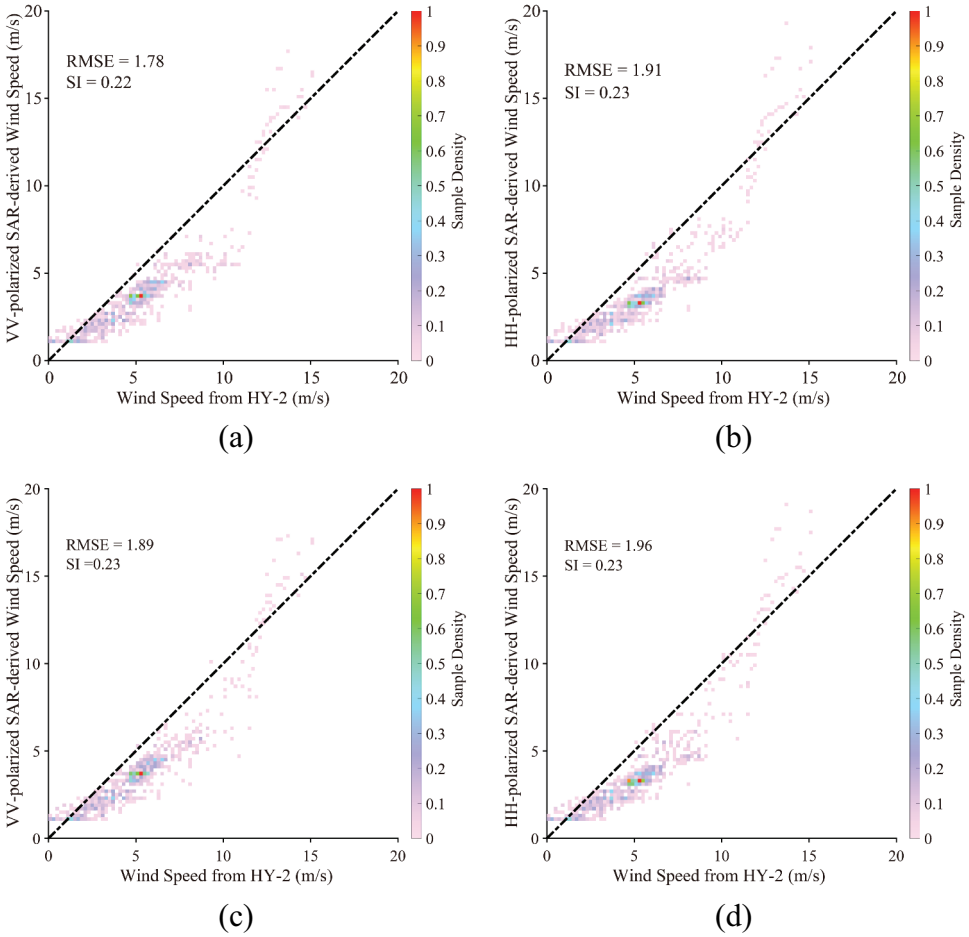

Figure 9. Comparison of wind speed retrievals with the measurements from HY-2 scatterometer: (a) VV-polarization and (b) HH-polarization by 256×256 sub-scenes; (c) VV-polarization and (b) HH-polarization by 512×512 sub-scenes.

retrievals increase. The sub-scenes with different spatial grid extracted from image are collocated with the swath data of HY-2 scatterometers, and more than 1000 matchups are available for validation, as exhibited in Figure 9, i.e. Figures 9(a,b) by 256 × 256 sub-scenes and Figures 9(c,d) by 512 × 512 sub-scenes, respectively. It is observed that RMSE of VV-polarized SAR-derived wind speeds by 256 × 256 sub-scenes is 1.78 m/s with a 0.22 SI (Figure 9(a)), which is better than a 1.91 m/s RMSE of HH-polarized SAR-derived wind speeds with a 0.22 SI (Figure 9(b)). It is reasonable that sea surface roughness is more sensitive with VV-polarized backscattering signal than that in HH-polarization. However, there is apparent underestimation of SAR wind retrieval. This behavior is also found in the comparison of SAR retrievals by 512 × 512 sub-scenes, i.e. a 1.89 m/s with a 0.23 SI for VV-polarization (Figure 9(c)) and a 1.96 m/s with a 0.23 SI for HH-polarization (Figure 9(c)). We think this is probably caused by inaccurate calibration of 1mC-SAR image, and the spatial grid is also an important issue for wind retrieval.

Validation of wave retrieval

The wave slop spectrum is retrieved from images by polarimetric technique taking SAR-derived wind. As an example, Figure 10(a) depicts the sub-scene of 256 × 256 extracted at the red rectangle in Figure 1 (a), i.e., (a) VV-polarization, (b) HH-polarization, (c) HV-polarization and (d) polarization orientation of 45°. The two-dimensional SAR slop spectrum is shown in Figure 11(a), and the one-dimensional SAR-derived wave slop spectrum are illustrated in Figure 11 (b). In this case, the SAR-derived SWH is 0.76 m, which is close to a 0.81 m from WW3. Figure 12 shows the comparison of collocated SWH with the WW3 simulations, yielding a 0.53 m RMSE with a 0.36 SI. Simultaneously, SAR-derived wave spectra are compared with WW3-simulated wave spectra, yielding a 0.79 Cor and a 0.92 Err.

Discussion

Figure 13 shows the variation in the wind speed relative to the measurements from HY-2 scatterometers, in which the Figures 13(a,b) represent the bias

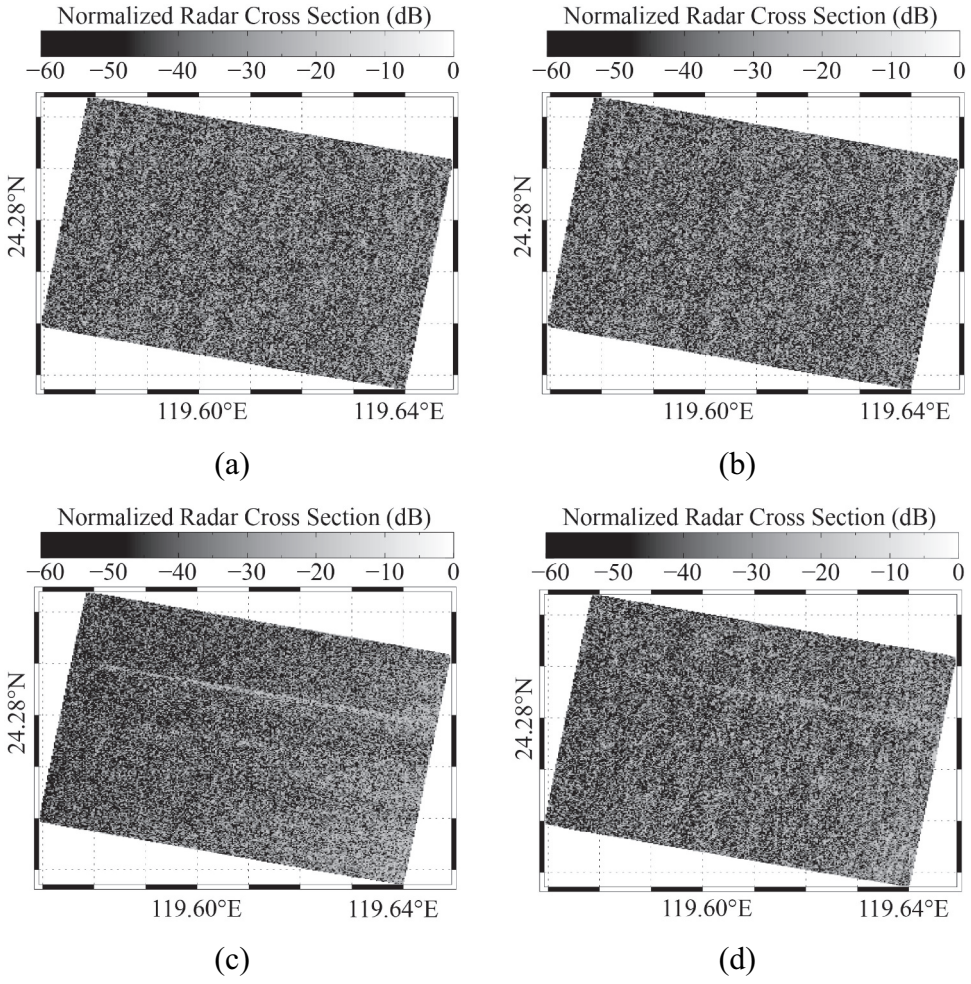

Figure 10. The sub-scene of 256 × 256 extracted at red rectangle in Figure 1a, i.e., (a) VV-polarization, (b) HH-polarization, (c) HV-polarization and (d) polarization orientation of 45°.

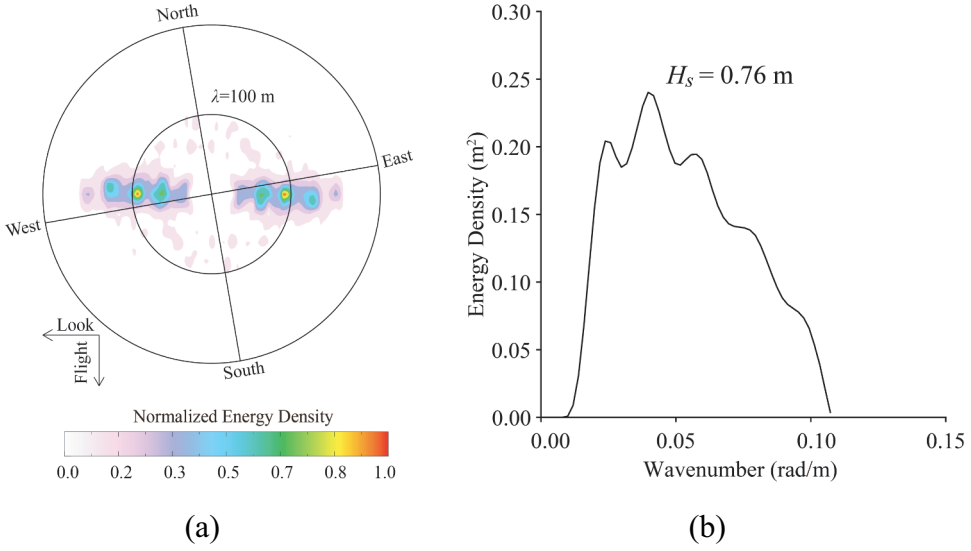

Figure 11. (a) The two-dimensional SAR slop spectrum and (b) one-dimensional SAR-derived wave slop spectrum.

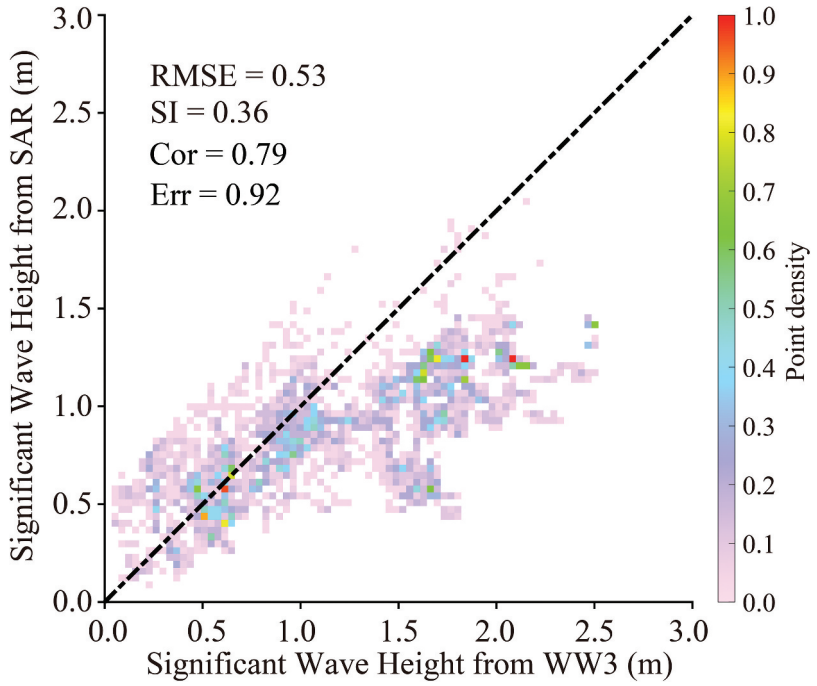

Figure 12. Comparison of SAR retrievals with the SWHs simulated by WW3.

between SAR retrievals in VV-polarization and HH-polarization minus the measurements from HY-2 scatterometers. The bias is grouped into bins of 1 m/s wind speed, and the bias increases with increasing wind speed from 2 m/s. However, the bias decreases with wind speed greater than 10 m/s. Similarly, the variation in the SAR retrievals relative to SWHs from WW3 for a bin 0.2 m of SWH is presented in Figure 14, indicating an increasing tendency with growth of sea state. This behavior is consistent with the variation in wind speed because the error of wind speed is inherent in the tilt MTF used in polarimetric technique.

Conclusions

The successor of GF-3 with spatial resolution up to 1 m, called 1mC-SAR, operationally starts releasing data since 2023. In our work, the preliminary analysis of wind and wave retrieval from 1mC-SAR image is conducted so as to confirm the applicability of 1mC-SAR for upper oceanic dynamics monitoring. In particular, the updated tilt MTFs considering the term of wind are implemented in polarimetric technique for SAR wave retrieval.

More than 400 images acquired in QPS mode are collected at China coastal waters during the period of April 2023. Wind directions are obtained from

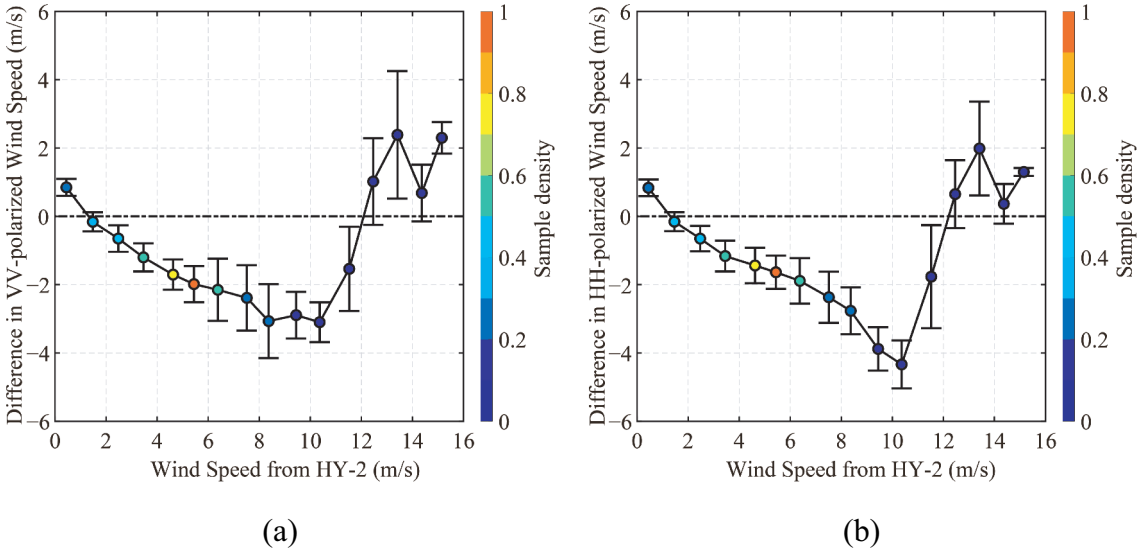

Figure 13. The variation in the wind speed relative to the measurements from HY-2 scatterometers: (a) VV-polarization and (b) HH-polarization. The bias is grouped into bins of 1 m/s wind speed.

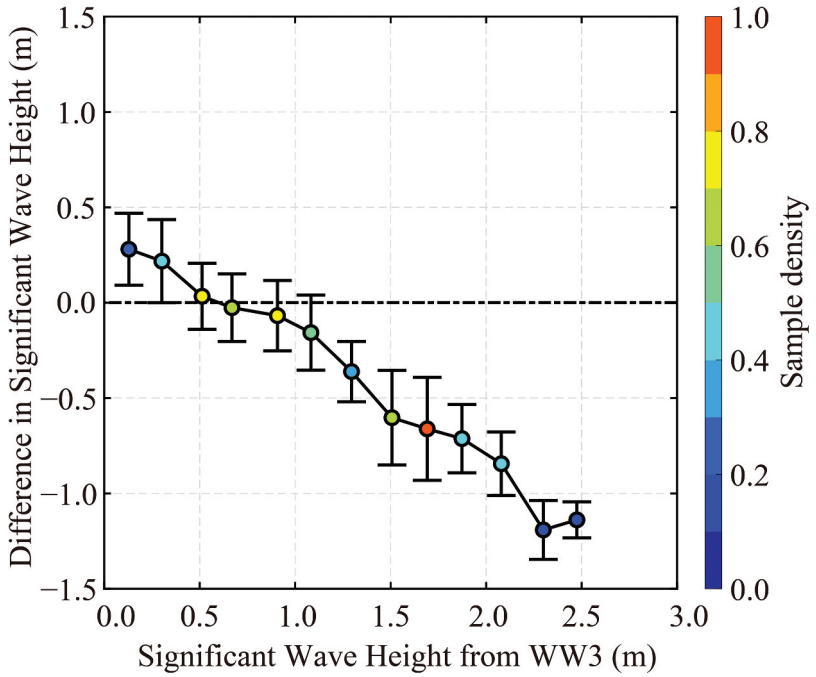

Figure 14. The variation in the SWH relative to the WW3 simulations, in which the bias is grouped into bins of 0.2 m SWH.

images when employing ERA-5 data. Then co-polarized GMF CSARMOD-GF is used for SAR wind speed retrieval, in which wind direction and incidence angle are taken as prior information. Wind speed retrievals are collocated with the measurements from HY-2 scatterometers, and comparisons yield a 1.78/1.91 m/s RMSE with a 0.22/0.23 SI in VV/HH-polarization. It is believed that the underestimation of SAR wind retrievals is caused by inaccurate calibration of image. In addition, it was found that the accuracy of SAR-derive winds by 256×256 sub-scenes is relatively higher than that gained from the results by 512×512 sub-scenes. Afterwards, the wave spectrum is inverted from SAR intensity spectrum by polarimetric technique with updated tilt MTF. Validation against the simulated SWHs from WW3 concludes the accuracy of VV-polarized retrievals is comparable, i.e. 0.53 m RMSE with a 0.36 SI. This result is also found in the comparison of wave spectra with WW3 simulations, i.e. a 0.79 Cor with a 0.92 Err. However, the bias of SWH indicates an increasing tendency with the growth of sea state, which is consistent with the variation of bias in wind speed. This is probably caused by the inaccurate wind speed used in tilt MTF.

It is supposedly that the calibration of 1mC-SAR necessitates to be improved. In the future, the TC can be simultaneously monitored by HY-2, CFOSAT and

1mC-SAR, and this campaign brings a precious opportunity to conduct TC dynamics research based on multi-source satellites.

Acknowledgments

We truly appreciate the provisions of 1mC-SAR image and the product from Haiyang-2B/2C/2D (HY-2B/2C/2D) by the National Ocean Satellite Application Center (NSOAS) via https://osdds.nsoas.org.cn. We also thank for the National Center for Environmental Prediction (NCEP) of National Oceanic and Atmospheric Administration (NOAA) providing the source code for the WAVEWATCH-III (WW3) model free of charge. The wind data provided by the European Centre for Medium-Range Weather Forecasts (ECMWF) is collected via http://www.ecmwf.int. Water depth released by General Bathymetry Chart of the Oceans (GEBCO) are downloaded via ftp.edcftp.cr.usgs.gov.

Disclosure statement

No potential conflict of interest was reported by the author(s).

Funding

This research was funded by the National Key Research and Development Program of China [2023YFE0102400], the National Natural Science Foundation of China [42076238 and 42376174], and the Natural Science Foundation of Shanghai [23ZR1426900].

ORCID

Wei-Zeng Shao http://orcid.org/0000-0003-3693-6217

Data availability statement

Due to the nature of this research, participants of this study did not agree for their data to be shared publicly, so supporting data are not available.

References

Alpers, W., & Bruning, C. (1986). On the relative importance of motion-related contributions to SAR imaging mechanism of ocean surface waves. *IEEE Transactions on Geoscience and Remote Sensing*, *24*(6), 873–885. https://doi.org/10.1109/TGRS.1986.289702

Corcione, V., Grieco, G., Portabella, M., Nunziata, F., & Migliaccio, M. (2018). A novel Azimuth cutoff implementation to retrieve sea surface wind speed from SAR imagery. *IEEE Transactions on Geoscience and Remote Sensing*, *57*(6), 3331–3340. https://doi.org/10.1109/TGRS.2018.2883364

Gao, Y., Sun, J., Zhang, J., & Guan, C. L. (2021). Extreme wind speeds retrieval using sentinel-1 IW mode SAR data. *Remote Sensing*, *13*(10), 1867. https://doi.org/10.3390/rs13101867

Grieco, G., Lin, W., Migliaccio, M., Nirchio, F., & Portabella, M. (2016). Dependency of the sentinel-1 azimuth wavelength cut-off on significant wave height and wind speed. *International Journal of Remote Sensing*, *37*(21), 5086–5104. https://doi.org/10.1080/01431161.2016.1226525

Grieco, G., Nirchio, F., & Migliaccio, M. (2015). Application of state-of-the-art SAR X-band geophysical model functions (GMFs) for sea surface wind (SSW) speed retrieval to a data set of the Italian satellite mission COSMO-SkyMed. *International Journal of Remote Sensing*, *36*(9), 2296–2312. https://doi.org/10.1080/01431161.2015.1034893

Hao, M. Y., Shao, W. Z., Shi, S. H., Liu, X., Hu, Y. Y., & Zuo, J. C. (2023a). Validation of surface waves investigation and monitoring data against simulation by simulating waves nearshore and wave retrieval from Gaofen-3 synthetic aperture radar image. *Remote Sensing*, *15*(18), 4402. https://doi.org/10.3390/rs15184402

Hao, M. Y., Shao, W. Z., Yao, R., Zhang, Y. G., & Jiang, X. W. (2023b). Improvement of quad-polarized velocity bunching modulation transfer function by C-band Gaofen-3 SAR. *Remote Sensing Letters*, *14*(9), 970–980. https://doi.org/10.1080/2150704X.2023.2255347

Hasselmann, K., & Hasselmann, S. (1991). On the nonlinear mapping of an ocean wave spectrum into a synthetic aperture radar image spectrum and its inversion. *Journal of Geophysical Research*, *96*(C6), 10713–10729. https://doi.org/10.1029/91JC00302

Hersbach, H., Stoffelen, A., & Haan, S. D. (2007). An improved C-band scatterometer ocean geophysical model function: CMOD5. *Journal of Geophysical Research Oceans*, *112*(C3), C03006. https://doi.org/10.1029/2006JC003743

He, Y., Shen, H., & Perrie, W. (2006). Remote sensing of ocean waves by Polarimetric SAR. *Journal of Atmospheric and Oceanic Technology*, *23*(12), 1768–1773. https://doi.org/10.1175/JTECH1948.1

Hu, Y. Y., Shao, W. Z., Shen, W., Zhou, Y., & Jiang, X. W. (2023). Machine learning applied to a dual-polarized Sentinel-1 image for wind retrieval of tropical cyclones. *Remote Sensing*, *15*(15), 3948. https://doi.org/10.3390/rs15163948

Jiang, T., Shao, W. Z., Hu, Y. Y., Zheng, G., & Shen, W. (2023). L-band analysis of the effects of oil slicks on sea wave characteristics. *Journal of Ocean University of China*, *22*(1), 9–20. https://doi.org/10.1007/s11802-023-5172-x

Ji, Q. Y., Shao, W. Z., Sheng, Y. Z., Yuan, X. Z., Sun, J., Zhou, W., & Zuo, J. C. (2018). A promising method of typhoon wave retrieval from Gaofen-3 synthetic aperture radar image in VV-Polarization. *Sensors*, *18*(7), 2064. https://doi.org/10.3390/s18072064

Keller, W. C., & Wright, J. W. (1975). Microwave scattering and the straining of wind-generated waves. *Radio Science*, *10*(2), 139–147. https://doi.org/10.1029/RS010i002p00139

Kerbaol, V., Chapron, B., & Vachon, P. W. (1998). Analysis of ERS-1/2 synthetic aperture radar wave mode imagettes. *JGR Oceans*, *103*(C4), 7833–7846. https://doi.org/10.1029/97JC01579

Lai, Z. Z., Hao, M. Y., Shao, W. Z., Shen, W., Hu, Y. Y., & Jiang, X. W. (2023). Wind field reconstruction based on dual-polarized synthetic aperture radar during a tropical cyclone. *European Journal of Remote Sensing*, *56*(1), 2273867. https://doi.org/10.1080/22797254.2023.2273867

Li, X. M., Konig, T., Schulz-Stellenfleth, J., & Lehner, S. (2010). Validation and intercomparison of ocean wave spectra inversion schemes using ASAR wave mode data. *International Journal of Remote Sensing*, *31*(17), 4969–4993. https://doi.org/10.1080/01431161.2010.485222

Li, X. M., Lehner, S., & Bruns, T. (2011). Ocean wave integral parameter measurements using envisat ASAR

wave mode data. *IEEE Transactions on Geoscience and Remote Sensing*, *49*(1), 155–174. https://doi.org/10.1109/TGRS.2010.2052364

Long, D. G., & Mendel, J. M. (1991). Identifiability in wind estimation from scatterometer measurements. *IEEE Transactions on Geoscience and Remote Sensing*, *29*(2), 268–276. https://doi.org/10.1109/36.73668

Lu, Y., Zhang, B., Perrie, W., Li, X. F., & Wang, H. (2018). A C-band geophysical model function for determining coastal wind speed using synthetic aperture radar. *IEEE Journal of Selected Topics in Applied Earth Observations and Remote Sensing*, *11*(7), 2417–2428. https://doi.org/10.1109/JSTARS.2018.2836661

Mastenbroek, C., & Valk, C. F. D. (2000). A semi-parametric algorithm to retrieve ocean wave spectra from synthetic aperture radar. *Journal of Geophysical Research*, *105*(C2), 3497–3516. https://doi.org/10.1029/1999JC900282

Migliaccio, M., & Reppucci, A. (2006). A review of sea wind vector retrieval by means of microwave remote sensing. *Proceedings of the European Microwave Association*, *2*, 136–140.

Mouche, A. A., Chapron, B., Zhang, B., & Husson, R. (2017). Combined Co-and cross-polarized SAR measurements under extreme wind conditions. *IEEE Transactions on Geoscience and Remote Sensing: A Publication of the IEEE Geoscience and Remote Sensing Society*, *55*(12), 6746–6755. https://doi.org/10.1109/TGRS.2017.2732508

Mouche, A. A., Collard, F., Chapron, B., Dagestad, K. F., Guitton, G., Johannessen, J. A., Kerbaol, V., & Hansen, M. W. (2017). On the use of Doppler shift for sea surface wind retrieval from SAR. *IEEE Transactions on Geoscience and Remote Sensing: A Publication of the IEEE Geoscience and Remote Sensing Society*, *50*(7), 2901–2909. https://doi.org/10.1109/TGRS.2011.2174998

Pleskachevsky, A., Tings, B., Wiehle, S., Imber, J., & Jacobsen, S. (2022). Multiparametric sea state fields from synthetic aperture radar for maritime situational awareness. *Remote Sensing of Environment*, *280*(10), 113200. https://doi.org/10.1016/j.rse.2022.113200

Portabella, M., Stoffelen, A., & Johannessen, J. A. (2002). Toward an optimal inversion method for synthetic aperture radar wind retrieval. *Journal of Geophysical Research Oceans*, *107*(C8), 1–1. https://doi.org/10.1029/2001JC000925

Quilfen, Y., Chapron, B., Elfouhaily, T., Katsaros, K., & Tournadre, J. (1998). Observation of tropical cyclones by high-resolution scatterometry. *Journal of Geophysical Research Oceans*, *103*(C4), 7767–7786. https://doi.org/10.1029/97JC01911

Schulz-Stellenfleth, J., Lehner, S., & Hoja, D. (2005). A parametric scheme for the retrieval of two-dimensional ocean wave spectra from synthetic aperture radar look cross spectra. *Journal of Geophysical Research*, *101*(C5), 297–314. https://doi.org/10.1029/2004JC002822

Shao, W. Z., Hu, Y. Y., Jiang, X. W., & Zhang, Y. G. (2023). Wave retrieval from quad-polarized Chinese Gaofen-3 SAR image using an improved tilt modulation transfer function. *Geo-Spatial Information Science*, 1–19. https://doi.org/10.1080/10095020.2023.2239849

Shao, W. Z., Hu, Y. Y., Nunziata, F., Corcione, V., Li, X. M., & Li, X. (2020). Cyclone wind retrieval based on X-band SAR-derived wave parameter estimation. *Journal of Atmospheric and Oceanic Technology*, *37*(10), 1907–1924. https://doi.org/10.1175/JTECH-D-20-0014.1

Shao, W. Z., Jiang, T., Jiang, X. W., Zhang, Y. G., & Zhou, W. (2021a). Evaluation of sea surface winds and waves retrieved from the Chinese HY-2B data. *IEEE Journal of Selected Topics in Applied Earth Observations and Remote Sensing*, *14*(10), 9624–9635. https://doi.org/10.1109/JSTARS.2021.3112760

Shao, W. Z., Jiang, X. W., Sun, Z. F., Hu, Y. Y., Marino, A., & Zhang, Y. G. (2022a). Evaluation of wave retrieval for Chinese Gaofen-3 synthetic aperture radar. *Geo-Spatial Information Science*, *25*(2), 229–243. https://doi.org/10.1080/10095020.2021.2012531

Shao, W. Z., Nunziata, F., Zhang, Y. G., Corcione, V., & Migliaccio, M. (2021b). Wind speed retrieval from the Gaofen-3 synthetic aperture radar for VV- and HH-polarization using a Re-tuned algorithm. *European Journal of Remote Sensing*, *54*(1), 1318–1337. https://doi.org/10.1080/22797254.2021.1924082

Shao, W. Z., Zhao, C., Jiang, X. W., Wang, W. L., Shen, W., & Zuo, J. C. (2022b). Preliminary analysis of wave retrieval from Chinese Gaofen-3 SAR imagery in the Arctic Ocean. *European Journal of Remote Sensing*, *55*(1), 440–452. https://doi.org/10.1080/22797254.2022.2098830

Shao, W. Z., Zhu, S., Sun, J., Yuan, X. Z., Sheng, Y. X., Zhang, Q. J., & Ji, Q. Y. (2019). Evaluation of wind retrieval from Co-polarization Gaofen-3 SAR imagery around China seas. *Journal of Ocean University of China*, *18*(1), 84–96. https://doi.org/10.1007/s11802-019-3779-8

Stoffelen, A., & Anderson, D. (1997). Scatterometer data interpretation: Estimation and validation of the transfer function CMOD4. *Journal of Geophysical Research Oceans*, *102*(C3), 5767–5780. https://doi.org/10.1029/96JC02860

Stoffelen, A., Verspeek, J. A., Vogelzang, J., & Verhoef, A. (2017). The CMOD7 geophysical model function for ASCAT and ERS wind retrievals. *IEEE Journal of Selected Topics in Applied Earth Observations and Remote Sensing*, *10*(5), 2123–2134. https://doi.org/10.1109/JSTARS.2017.2681806

Stopa, J. E., & Mouche, A. (2017). Significant wave heights from Sentinel-1 SAR: Validation and applications. *Journal of Geophysical Research Oceans*, *122*(3), 1827–1848. https://doi.org/10.1002/2016JC012364

Sun, J., & Guan, C. L. (2006). Parameterized first-guess spectrum method for retrieving directional spectrum of swell-dominated waves and huge waves from SAR Images. *Chinese Journal of Oceanology and Limnology*, *24*(1), 12–20. https://doi.org/10.1007/BF02842769

Sun, Z. F., Shao, W. Z., Jiang, X. W., Nunziata, F., Wang, W. L., Shen, W., & Migliaccio, M. (2022). Contribution of breaking wave on the co-polarized backscattering measured by the Chinese Gaofen-3 SAR. *International Journal of Remote Sensing*, *43*(4), 1384–1408. https://doi.org/10.1080/01431161.2021.2009150

Wang, H., Yang, J. S., Lin, M. S., Li, W. W., Zhu, J. H., Ren, L., & Cui, L. M. (2022). Quad-polarimetric SAR sea state retrieval algorithm from Chinese Gaofen-3 wave mode imagettes via deep learning. *Remote Sensing of Environment*, *273*(3), 112969. https://doi.org/10.1016/j.rse.2022.112969

WAVEWATCH III Development Group. (2019). *User manual and system documentation of WAVEWATCH III version 6.07*. National Oceanic and Atmospheric Administration.

Yang, X. F., Li, X. F., Pichel, W., & Li, Z. W. (2011). Comparison of ocean surface winds from ENVISAT ASAR, metop ASCAT Scatterometer, buoy measurements, and NOGAPS model. *IEEE Transactions on Geoscience and Remote Sensing*, *49*(12), 4743–4750. https://doi.org/10.1109/tgrs.2011.2159802

Yao, R., Shao, W. Z., Zhang, Y. G., Wei, M., Hu, S., & Zuo, J. C. (2023). Feasibility of wave simulation in typhoon using WAVEWATCH-III forced by remote-sensed wind.

Journal of Marine Science and Engineering, *11*(10), 2010. https://doi.org/10.3390/jmse11102010

Zhang, G. S., Li, X. F., Perrie, W., Hwang, P., Zhang, B., & Yang, X. F. (2017). A hurricane wind speed retrieval model for C-Band RADARSAT-2 cross-polarization ScanSAR images. *IEEE Transactions on Geoscience and Remote Sensing*, *55*(8), 4766–4774. https://doi.org/10.1109/TGRS.2017.2699622

Zhang, Y. M., Wang, Y. H., Zhang, J., & Liu, Y. Z. (2021). Reanalysis of the tilt MTFs based on the C-Band empirical geophysical Model function. *IEEE Geoscience & Remote Sensing Letters*, *18*(9), 1500–1504. https://doi.org/10.1109/LGRS.2020.3004332

Zhang, Y., Wang, Y. H., Zhang, J., & Liu, Y. Z. (2020). Reanalysis of the tilt MTFs based on the C-band empirical geophysical model function. *IEEE Geoscience and Remote Sensing Letters*, *18*(9), 1500–1504. https://doi.org/10.1109/LGRS.2020.3004332

Zhao, X. B., Shao, W. Z., Hao, M. Y., & Jiang, X. W. (2023). Novel approach to wind retrieval from sentinel-1 SAR in tropical cyclones. *Canadian Journal of Remote Sensing*, *49*(1), 2254839. https://doi.org/10.1080/07038992.2023.2254839

Zhong, R. Z., Shao, W. Z., Zhao, C., Jiang, X. W., & Zuo, J. C. (2023). Analysis of wave breaking on Gaofen-3 and TerraSAR-X SAR image and its effect on wave retrieval. *Remote Sensing*, *15*(3), 574. https://doi.org/10.3390/rs15030574

Zhu, S., Shao, W. Z., Armando, M., Shi, J., Sun, J., Yuan, X. Z., Hu, J. C., Yang, D. K., & Zuo, J. C. (2018). Evaluation of Chinese quad-polarization Gaofen-3 SAR wave mode data for significant wave height retrieval. *Canadian Journal of Remote Sensing*, *44*(6), 588–600. https://doi.org/10.1080/07038992.2019.1573136

Zhu, S., Shao, W. Z., Marino, A., Sun, J., & Yuan, X. Z. (2020). Semi-empirical algorithm for wind speed retrieval from Gaofen-3 quad-polarization strip mode SAR data. *Journal of Ocean University of China*, *19*(1), 23–35. https://doi.org/10.1007/s11802-020-4215-9